Radiochim. Acta **100**, 605–614 (2012) / **DOI** 10.1524/ract.2012.1968

Two-mode fission – experimental verification and characterization of two fission-modes

By Y. Nagame[1,*] and H. Nakahara[2]

[1] Advanced Science Research Center, Japan Atomic Energy Agency, Tokai, Ibaraki 319-1195, Japan
[2] Department of Chemistry, Tokyo Metropolitan University, Hachioji, Tokyo 192-0397, Japan

(Received March 30, 2012; accepted in revised form May 31, 2012)
(Published online July 30, 2012)

Two-mode fission / Symmetric fission / Asymmetric fission / Saddle-point configuration / Scission-point configuration / Bimodal fission

Summary. Experimental verification and characterization of the two-mode fission are reviewed. The presence of two independent deformation-paths in low energy fission of actinides is demonstrated by studying correlation among saddle-point configurations, scission-point configurations, and mass-yield distributions; the elongated scission configuration is related with the fission process that goes over a higher threshold energy and results in a symmetric mass-division mode, while the compact scission configuration with the process that experiences a lower threshold ends up with an asymmetric mass-division mode. Based on an extensive systematic analysis of scission properties in a wide range of actinide fission, the bimodal fission observed in the spontaneous fission of the heavy actinides is interpreted as the result of the presence of two fission paths, namely, the ordinary asymmetric fission path and a strongly shell-influenced symmetric mode.

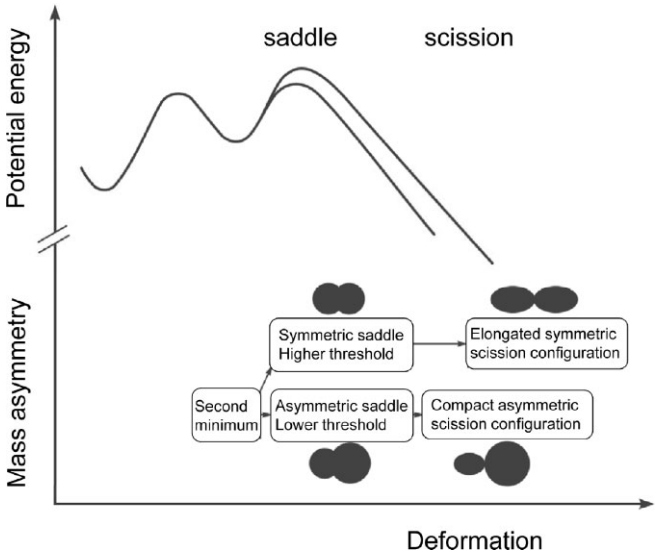

Fig. 1. A schematic drawing of variation of the potential energy surface in the low energy fission of actinides. Adapted from [7].

1. Introduction

Nuclear fission was discovered by Hahn and Strassmann in 1939 [1]. As discussed by Meitner and Frisch [2], and Bohr and Wheeler [3] just after the discovery, the fission process was described as an evolution of nuclear deformation from a spherical or deformed ground-state shape to an elongated dumbbell-like configuration that finally divides into two fragments with enormous energy release. Since then, a large number of experimental and theoretical investigations have been performed to understand this exotic mass-division mechanism, *e.g.* in [4–7]. A typical schematic feature of the deformation process in low-energy fission of actinides is shown in Fig. 1; mass asymmetry and potential energy are plotted as a function of deformation toward fission axis. A nucleus starts from a ground state and over the first (inner) barrier passes through the second minimum. The preference for asymmetric mass-division in low-energy fission of light and medium actinides has been a big puzzle in the study of fission mechanism. According to theoretical calculations, the asymmetric mass-division is closely related with the reflection asymmetric configuration of a saddle-point at the outer barrier in the potential energy surfaces [8, 9]. The probability of choosing either path is decided by the barrier heights and level densities at each outer barrier, and neutron and proton shell structures of fissioning nuclei [10].

Two independent deformation-paths from saddle to scission in fission were first hypothesized by Turkevich and Niday [11] as two-mode fission to interpret the incident energy dependence of symmetric and asymmetric mass-division products. Information about the saddle has been extensively studied by measuring angular distributions and excitation functions of fission products. The presence of two kinds of fission barriers (threshold energies) in the deformation process has been experimentally confirmed by several authors, such as [12–20]; the fission process that experiences the higher threshold energy leads to the fragment mass distribution centered around the half-mass of a fissioning nucleus, while the lower threshold process leads to

*Author for correspondence (Email: nagame.yuichiro@jaea.go.jp).
This author is a member of the Editorial Advisory Board of this journal. Editor

the asymmetric mass-distribution. On the other hand, information on scission configurations has been obtained from fragment kinetic energies and mass-yield distributions influenced by shell structures of fragments near scission [21, 22]. The existence of at least two different scission configurations for the same mass-split was demonstrated by Balagna *et al.* [23] and Hulet *et al.* [24, 25] in the spontaneous fission (SF) of the heavy actinides. It is called bimodal fission; one is a shell-influenced compact fragment shape associated with high total kinetic energy (TKE) and the other one is an elongated liquid drop-like shape with low TKE. A correlation between the mass-yield curve and TKE of fragments was observed [24, 25]. Similar bimodal fission phenomena were also observed in the proton-induced fission of ^{232}Th through ^{248}Cm [26, 27] and the authors corroborated the presence of at least two kinds of scission configurations for certain mass division with fragment mass numbers around $A = 130$. The correlation between scission configurations and mass distributions has ascertained that elongated scission configurations are associated with the symmetric mass distribution and more compact scission configurations with the asymmetric mass distribution [26, 27]. The presence of two independent deformation-paths in low energy fission of actinides was demonstrated by studying the correlation among saddle-point configurations, scission-point configurations and mass-yield distributions [7, 28–30]. This is essentially experimental verification and further extension of the working hypothesis of the two-mode fission by Turkevich and Niday [11]. The two deformation paths are characterized as schematically shown in Fig. 1. The first path is initiated with a higher fission barrier and ends with an elongated scission-configuration, giving a final mass-yield distribution centered near the half of the mass number of the fissioning nucleus, the symmetric fission path. In the second path, a fissioning nucleus experiences a lower fission barrier, resulting in a more compact scission-configuration, which gives a double humped mass-yield distribution always centered around the heavier fragment mass number $A = 140$, the asymmetric fission path. The above picture has been well reproduced by recent theoretical calculations of the potential energy surfaces by Möller *et al.* [31]; the saddle leading to the mass-symmetric division is found to be a few MeV higher than that to the mass-asymmetric division, and the compact scission-configuration is related to the asymmetric fission whereas the elongated one is associated with the symmetric fission path. The clear ridge separating the two fission valleys, symmetric and asymmetric, is also demonstrated [31]. The presence of two static fission paths leading to different scission configurations separated by ridges was also theoretically pointed out for the fission of actinides [32, 33].

In this article, experimental verification and characterization of the two-mode fission are reviewed in Sects. 2–4. Then, we summarize characteristics of the deformation properties of the symmetric and asymmetric scission-configurations in Sect. 5 that are evaluated from experimental fragment TKE and neutron multiplicity (ν), the number of neutrons emitted from fission fragments. Based on an extensive systematic analysis of deformation properties at scission in a wide range of fissioning nuclei, an interpretation of the so-called bimodal fission observed in SF of the heavy actinides is presented in Sect. 6. Scission properties in the fission of light actinides and those of the heavy actinides are briefly discussed.

2. Two kinds of threshold energies – two kinds of saddle-point configurations

2.1 Excitation function of fission products

It is well known that the yields of symmetric mass-division products increase more rapidly as a function of incident projectile energy than those of asymmetric mass-division products in low-energy fission of actinides. Fig. 2 shows ratios of the production cross sections of the typical asymmetric fission product, ^{143}Ce, and symmetric one, ^{105}Rh, to that of symmetric mass-division products (σ_{sym}: an average cross section of fragment mass number $A = 112$ and 115) as a function of the incident proton energy in the fission of ^{232}Th [15]. For ^{143}Ce, the ratio decreases with a local minimum at the proton energy around 14 MeV, while no clear energy dependence is observed for ^{105}Rh. This means that the energy dependence of the cross sections for the asymmetric mass-division product and that for the symmetric one is quite different. It was also found that the energy dependence is the same within each mass-division group [15, 18–20]. Application of the Bohr-Wheeler type statistical model to the analysis of these excitation functions gives two kinds of fission barrier heights (threshold energies), the barrier height for the symmetric mass-division being a few MeV higher than that for the asymmetric one in the region of light actinides [15, 20]. The difference between the two barriers (threshold energies) as a function of neutron number of the fissioning nuclei is shown in Fig. 3 for a wide range of actinides [20]. The data in the light mass region are taken from [14, 34, 35]. The difference ($B_f^s - B_f^a$) changes systematically from a positive value at neutron number $N \sim 150$ to a negative one at $N \sim 126$, and the two barriers become comparable at around $N = 136$, where B_f^s indicates the fission barrier of symmetric mass-division and B_f^a of asymmetric one.

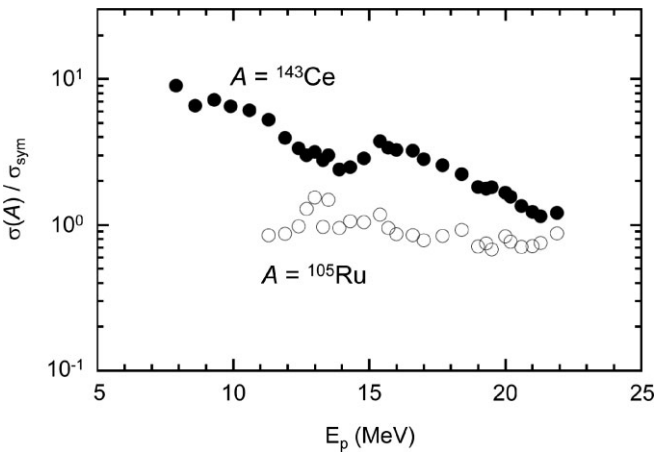

Fig. 2. Typical cross section ratios $\sigma(A)/\sigma_{sym}$ as a function of the incident particle energy in the proton-induced fission of ^{232}Th [15]. Adapted from [29]. Closed and open circles show the ratios of $\sigma(^{143}\text{Ce})/\sigma_{sym}$ and $\sigma(^{105}\text{Rh})/\sigma_{sym}$, respectively.

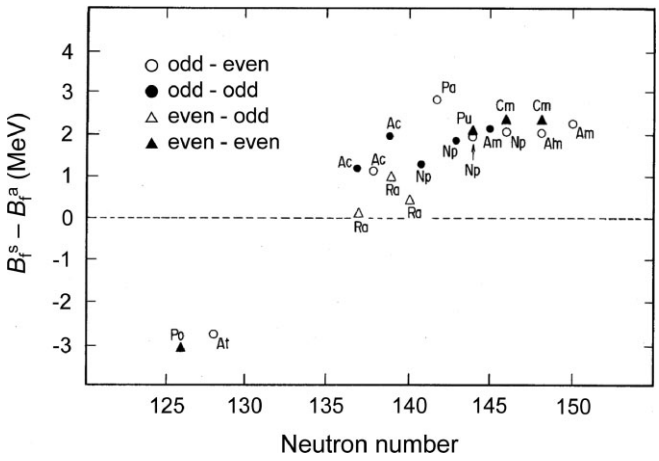

Fig. 3. Difference in the barrier heights (threshold energies) between symmetric (B_f^s) and asymmetric (B_f^a) mass-divisions as a function of neutron number of the various fissioning nuclides. Adapted from [20].

2.2 Correlation between angular anisotropy and mass distribution

The existence of separate saddle-point configurations for each symmetric and asymmetric mass division was also verified with the data on fragment mass dependence of angular anisotropies expressed by W(180°)/W(90°) [12, 16, 36, 37]. According to the transition state theory [38, 39], angular distributions of fission fragments are determined by the saddle-point nuclear shape. If the modes of mass-division correspond to different saddle-point configurations, a correlation is expected between angular anisotropy and mass distribution of fission products.

The typical experimental result on the correlation between angular anisotropy and mass distribution is displayed in Fig. 4 for the 15 MeV proton-induced fission of ^{232}Th [16, 40]. A clear dependence of the angular anisotropy on the fragment mass number is seen; the anisotropies of the symmetrically divided products are considerably smaller than those of the asymmetrically divided ones.

From the above data on excitation functions and angular distributions of the products, the existence of the two fission-modes with two types of entrance channels (saddle-point configurations) in fission has been revealed.

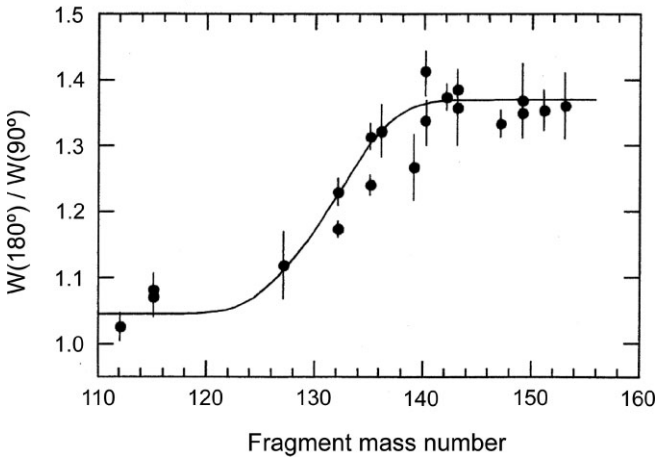

Fig. 4. Correlation between angular anisotropy and fragment mass number in the 15 MeV proton-induced fission of ^{232}Th. Adapted from [16, 40].

3. Two kinds of scission configurations – two kinds of fragment deformation at scission

3.1 Total kinetic energy (TKE) distribution of fission fragments

The existence of two distinctively different scission configurations for the same mass division was demonstrated in SF of the heavy actinides [23–25]. The most striking and significant features are that the mass-yield distribution is essentially single-peaked around the symmetric mass-split, resulting in products with the mass number $A \sim 130$, whereas the TKE distribution apparently exhibits the structure with a shoulder that strongly suggests the presence of at least two components in the TKE distribution. As typical data, the TKE and mass-yield distributions observed in SF of ^{260}Md [41] are depicted in Fig. 5a,b, respectively; two components are clearly seen in the TKE distribution. The two-component analysis showed that the high-TKE events mostly constitute the sharp mass-yield curve around the symmetry and the low-TKE ones a broad flat-topped distribution. The neutron multiplicity (ν) distributions in correlation with TKE of the fragments were also measured and a large drop in the number of neutrons emitted from the high-TKE component was observed (dashed histogram in Fig. 5c), implying that the fragments with the high-TKE component are less deformed while those with low-TKE are largely deformed at scission [41]. The authors called the fission with such phenomena as bimodal fission. It should be noted that the high-TKE component ($\sim$ 235 MeV) in the symmetric mass division was first shown in SF of ^{257}Fm by Balagna *et al.* [23, 42]. The correlation among the neutron multiplicity, fragment TKE and mass-yield distributions in the various SF systems was also vigorously investigated by Hoffman *et al.* [43].

Bimodal fission phenomena were observed even in the light actinide fission. In the low energy proton-induced fission of ^{232}Th through ^{248}Cm, two components in the TKE distributions were verified by double time-of-flight (TOF) measurements of velocities of complementary fragments in the fragment mass region around 130 where the asymmetric mass-yield merges into the symmetric mass-yield [26, 27]. The two components were decomposed into low- and high-TKE ones. Assuming that TKE originates from the Coulomb repulsion energy between the two touching fragments at the scission point, the distance (D) between the two charge centers of complementary fragments is evaluated from the average TKE value, $\langle$TKE$\rangle$. The resulting D is plotted in Fig. 6a as a function of the heavier fragment mass number in the fission of ^{232}Th with 13 MeV protons [28]. The open and solid squares correspond to the distances obtained from the two-component analysis. It is obvious that there are two kinds of scission configurations; the first one is the compact scission shape (small D) and the other is the elongated one (large D) in the same mass-split around $A \sim 130$.

The intensity ratios of the two components in the TKE distributions were used to decompose the mass-yield distributions and the result is shown in Fig. 6b. The open squares

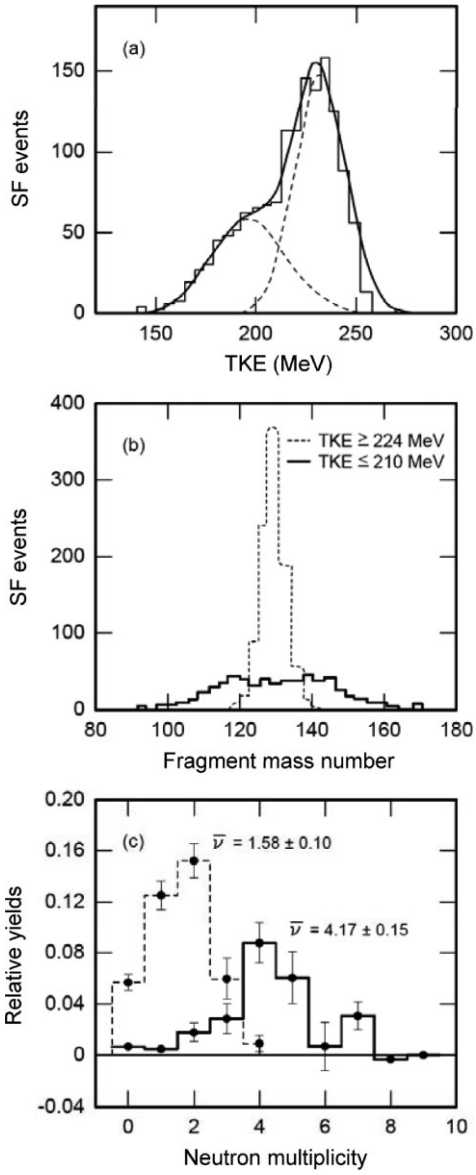

Fig. 5. (**a**) TKE distribution for spontaneous fission of ^{260}Md. (**b**) Decomposed mass-yield distributions for the events with TKE $\geq$ 224 MeV (dashed histogram) and for those with TKE $\leq$ 210 MeV (solid histogram). (**c**) Neutron multiplicity distributions; the dashed histogram is derived from the events with TKE $\geq$ 224 MeV and the solid histogram is those from TKE $\leq$ 210 MeV. Adapted from [41].

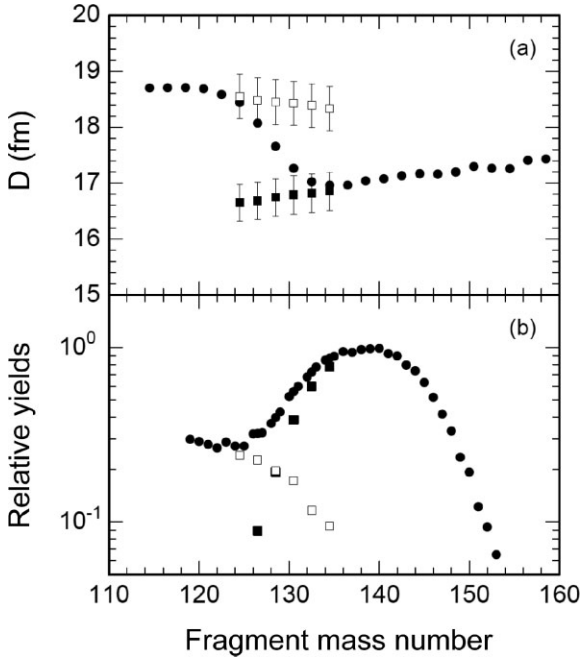

Fig. 6. (**a**) Distance of two charge centers at scission configurations evaluated from the average total kinetic energy of the fragment mass in the 13 MeV proton-induced fission of ^{232}Th. The closed circles show the distance estimated from the average total kinetic energy values. The closed and open squares indicate the distances corresponding to the two types of average kinetic energies. (**b**) Decomposed mass yield curves. The closed and open squares are the decomposed mass yields corresponding to the high- and low-TKE components, respectively. Adapted from [28].

show the mass yields corresponding to the low-TKE components while the solid squares are those to high-TKE. The figure indicates that the overall mass yield curve can be smoothly decomposed into the two components in the mass region $A \sim 130$. The correlation between the scission configurations and the mass-yield distributions reveals that the elongated scission-configuration is associated with the mass-symmetric fission process while the more compact scission-configuration is with the mass-asymmetric one in the fission of the actinides [7, 28–30].

3.2 Neutron multiplicity (ν) distribution – number of emitted neutrons from fission fragments

Neutron multiplicity (ν) distributions well indicate the fragment deformation at scission as discussed in Sect. 3.1. The average neutron multiplicity $\overline{\nu}$ was measured in coincidence with fragments in the 12 MeV proton-induced fission of ^{232}Th [44]. The $\overline{\nu}$ values obtained for each fission mode are shown in Fig. 7 for typical fragment pairs together with the TKE distributions. The left part shows $\overline{\nu}$ for the light fragments (A_L) and the right one those for the complementary heavy fragments (A_H). In the bottom left is shown the distribution for the symmetrically divided products with $A = 116$–117. For the typical asymmetric mass-division, $\overline{\nu}$ of the light fragments with $A_L = 88$–89 are considerably smaller than those of the complementary heavy fragments at the same TKE. This means that the heavier fragment has a much more excitation energy and is more deformed compared to the light fragment. The $\overline{\nu}$ values of $A_L = 102$–103 in the TKE region above 180 MeV (high-TKE) become larger than those of the complementary heavy fragments ($A_H = 130$–131), while $\overline{\nu}$ for the TKE below 170 MeV (low-TKE) is smaller than those of $A_H = 130$–131. In the latter energy region, $\overline{\nu}$ of the light fragment decreases as TKE becomes smaller whereas that of the heavier fragment rapidly increases. This indicates that in the fission events leading to high-TKE, *i.e.*, the asymmetric fission mode, the fragments with $A \sim 130$ are rather compact shaped while in those leading to low TKE, *i.e.*, the symmetric fission mode, the corresponding fragments are largely deformed. On the other hand, for the complementary light fragments with $A_L = 102$–103, no significant difference of $\overline{\nu}$ is observed between the high-TKE and low-TKE components.

In Fig. 8, the $\overline{\nu}$ values and the values corresponding to the symmetric ($\overline{\nu}_{sym}$) and asymmetric ($\overline{\nu}_{asym}$) fission modes

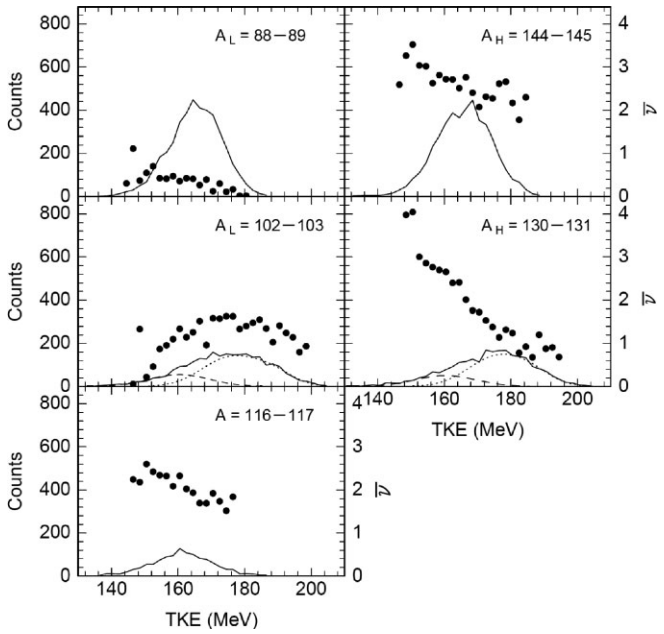

Fig. 7. Average neutron multiplicity $\overline{\nu}$ (solid circles) for the typical fragment pairs together with the TKE distributions in the 12 MeV proton-induced fission of ^{232}Th. For the fragments with $A = 102$–103 and 130–131, the TKE distributions are decomposed into the low- and high-TKE components that are shown by dashed and dotted curves, respectively. Adapted from [44].

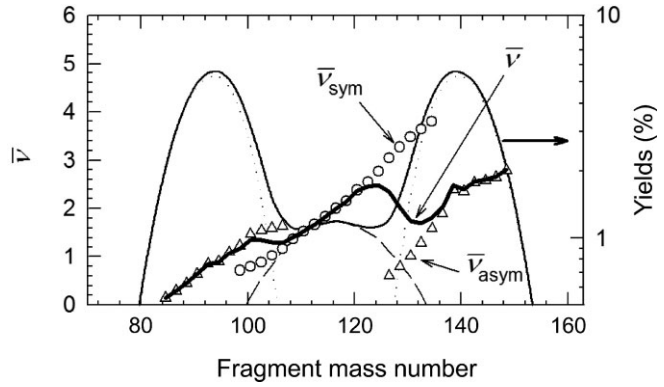

Fig. 8. Average neutron multiplicity $\overline{\nu}$ as a function of fragment mass number observed in the 12 MeV proton-induced fission of ^{232}Th. Open circles correspond to the symmetric fission mode and open triangles to the asymmetric one. Mass-yield curve is decomposed into the symmetric and asymmetric distributions that are shown by dashed and dotted curves, respectively. Adapted from [44].

are shown as a function of fragment mass number by thick solid line, open circles, and open triangles, respectively. The decomposed mass-yield distributions for each symmetric- and asymmetric-fission mode are also depicted by dashed and dotted lines, respectively. The structure of $\overline{\nu}$ at $A_L \sim 100$–110 and $A_H \sim 120$–130 is caused by the coexistence of the two fission-modes. The so-called saw-tooth structure observed in low-energy fission of actinides [45] is seen in $\overline{\nu}_{asym}$ with the local minima at around $A_L \sim 82$ and $A_H \sim 130$ that correspond to the fragment shells of nuclei with $N = 50$ and $Z = 50$ ($N = 82$) in the asymmetric fission, respectively. The $\overline{\nu}_{sym}$ value increases in a monotonous way with the fragment mass number and becomes largely different from the value of $\overline{\nu}_{asym}$. Based on these results, it is concluded that different kinds of scission configurations associated with the symmetric and asymmetric fission modes are strongly affected by different deformation properties of the heavy fragments with the mass number $A_H \sim 130$ compared with those of the complementary light fragments at $A_L \sim 100$. This means in the asymmetric fission mode the fragments show small deformation, thus retaining closed shell effects, while in the symmetric fission the fragments are largely deformed.

4. Correlation between saddle- and scission-point configurations

To verify the two independent fission paths from the saddle to scission, one has to see how the two kinds of scission configurations in the exit channel are correlated with the two types of threshold energies (fission barriers) in the entrance channel of fission. Double velocity TOF experiments for various incident energies were carried out and excitation functions of two kinds of the TKE components were constructed [28]. A typical comparison of the decomposed mass yields at different proton energies is shown in Fig. 9 for fission of ^{232}Th with protons of energies 14.7 MeV (closed symbols) and 12.0 MeV (open symbols). The yields at the peak top ($A \sim 140$) of the mass distributions are normalized to unity. A clear difference in the symmetric yields at around $A_f/2$ is observed between the two different incident energies (A_f: mass number of the fissioning nuclide), and the same amount of difference is also observed for the decomposed yields of the low-TKE components: the difference between open and closed triangles in Fig. 9. The result indicates that the excitation energy dependence of the yields for the low- and high-TKE components is quite different; the former is similar to that of the symmetric mass-division products while the latter to that of the asymmetric mass-division products. This excitation energy dependence leads us to conclude that in the low-energy fission of actinides the elongated scission-configuration is related to the fission process that requires the higher threshold energy and results

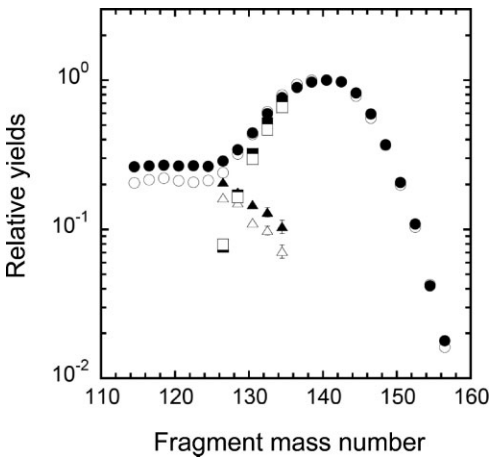

Fig. 9. Comparison of the decomposed mass yields in the 14.7 MeV (closed symbols) and 12.0 MeV (open symbols) proton-induced fission of ^{232}Th. The yields at the peak top ($A \sim 140$) are normalized to unity. The triangle symbols show the mass yields corresponding to the low-TKE components and the squares are those to high-TKE components. See the difference between open and closed triangles. Adapted from [28].

in the symmetric mass-division mode while the compact scission-configuration is related with the process that experiences the lower threshold and ends up with the asymmetric mass-division mode. The above picture is well reproduced by recent theoretical calculations of the five-dimensional potential energy surfaces by Möller *et al.* [31]; the saddle leading to the mass-symmetric division is found to be a few MeV higher than that to the mass-asymmetric division. The compact scission configuration is related to the asymmetric fission and the elongated one is associated with the symmetric fission path. The clear ridge separating the two symmetric and asymmetric fission valleys has also been pointed out [31, 46]. The presence of two static fission paths leading to different scission configurations separated by ridges was also described for the fission of actinides [32, 33]. Brosa *et al.* [33] suggested multi-fission valleys from saddle to scission influenced by shell-structure of fragments using random neck-rupture model: multi-mode fission.

5. Systematic features of the two-mode fission

5.1 Degree of fragment deformation at scission

We discuss the systematic variation of the elongated and compact scission-configurations in terms of shape elongation evaluated from the experimental TKE values including a large number of literature data (see [47, 48]). Here, Zhao *et al.* define the shape elongation parameter β which shows the degree of deformation at scission as $\beta = D/D_0$, where D_0 indicates the distance between charge centers of two touching spheres. The distance D is evaluated from $\langle$TKE$\rangle$ as described in Sect. 3.1.

The β_{asym} values for the scission-configurations leading to the asymmetric mass-division that produce the typical heavier fragment mass of $A_H = 140$ are plotted in Fig. 10a as a function of the mass number of the fissioning nuclide A_f. It is found that β_{asym} shows nearly the same value of 1.53 for both the particle-induced fission and SF, indicating that the degree of deformation at scission for the asymmetric fission mode is independent of the excitation energy (E^*) of fissioning nuclei. It is also interesting to note that the β_{asym} values evaluated from the low-TKE component in the bimodal fission (closed squares) are equal for both the pre-actinide and actinide region. The ordinary asymmetric fission mode passing through the asymmetric valley is evidently present even in the heavy actinide region. As discussed in Sect. 3.1, the fragments with low TKE seem to constitute the asymmetric mass distribution which has peaks around $A_L \sim 120$ and $A_H \sim 140$: see Fig. 5b.

Fig. 10b shows the β_{sym} values evaluated from the $\langle$TKE$\rangle$ data for the symmetric mass division of $A_1 = A_2 = A_f/2$. Obviously two extreme types of β_{sym} are present. The one is for the low-E^* fission in the region from the pre-actinide through the actinide until $A_f \sim 245$ (solid circles) and for the high-E^* fission (open circles) in a wide range of A_f, where β_{sym} is nearly constant at 1.65. It is noted that the β_{sym} value of 1.65 corresponds to that expected from the dynamical calculations of Davies *et al.* [49] based on the liquid drop model. This means that even though the symmetric barrier is influenced by the shell structure of a fissioning nucleus near the saddle, the degree of deformation and dynamics near the scission-point in the symmetric fission can be described by the liquid drop model. The other type of behavior is for SF in the region of $A_f \sim 260$, at which β_{sym} decreases to a constant value of 1.33 (open squares) which corresponds to that evaluated from the high-TKE component in the bimodal fission. The implied smaller elongation at scission would be related to the effects of spherical fragment shells of $Z = 50$ and $N = 82$ on the mass-symmetric deformation. Note that β_{sym} in the low-E^* fission and SF gradually becomes smaller beyond $A_f \sim 245$, approaching the value of 1.33; the shell effects on the scission shape in the symmetric fission valley are gradually manifested as a function of the neutron and proton numbers of the fissioning nuclides, although such effects do not appear in the fission that goes through the deformation path in the asymmetric fission valley. Thus, the feature of the symmetric fission mode, with the liquid-drop-like elongated scission configuration in the light actinides and pre-actinides, gradually shifts to that of the narrow symmetric mass distribution with the compact scission-configuration that is strongly affected by the spherical shell structure of $Z = 50$ and $N = 82$ for both the

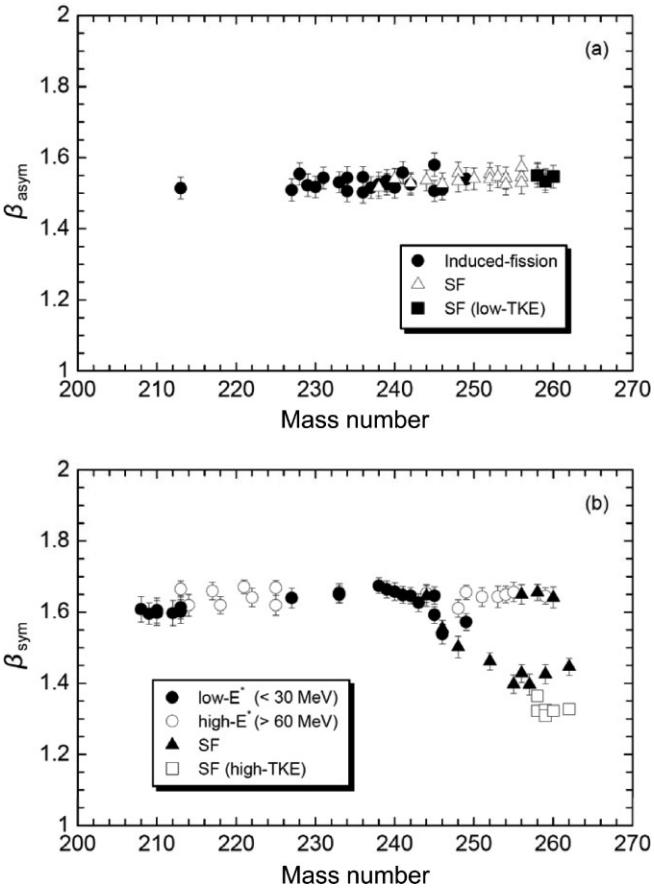

Fig. 10. (**a**) Shape elongation at scission for the asymmetric mass division as a function of the mass number of the fissioning nuclides A_f. Solid circles are results corresponding to the particle-induced fission while open triangles are for spontaneous fission. Solid squares are those corresponding to the low-TKE component observed in the bimodal fission of the heavy actinides. (**b**) Shape elongation for symmetric mass division as a function of A_f. Solid circles are the results for the low excitation fission ($E^* < 30$ MeV), while open circles are those for the high excitation fission ($E^* > 65$ MeV). Solid triangles are for SF and open squares show the results of the high-TKE component observed in the bimodal fission of the heavy actinide region. Adapted from [30, 47, 48].

complementary fragments. It is also found that due to washing out of shell effects in hot nuclei, β_{sym} in the high-E^* fission observed in $A_f \geq 245$ keeps the value of 1.65. There are also some SF data, ^{256,258,260}Rf ($N = 152, 154, 156$) [50], even in $A_f \geq 245$ that show $\beta_{sym} = 1.65$. At the extremely high-TKE or very small β_{sym}, the sudden change of the mass-yield curves to the symmetric narrow shape is obvious for the fissioning nuclides with the atomic number around 100 and the neutron number 160 [48]. The β_{sym} values (solid triangles) located in between β_{sym} = 1.65 and β_{sym} = 1.33 around A_f = 250 may be interpreted as a mixture of the high- and low-TKE components (no clear two components in the TKE distributions were observed in SF of ^{259}Lr [51] and ^{262}Rf [52]. It should be noted that the assignment of ^{262}Rf in [50] has been recently revised to the isomeric state of ^{261}Rf with the half-life of $\sim$ 2 s [53, 54]).

The systematic features of the β values in the fission of actinides have been well reproduced by theoretical calculations based on the two-center shell model coupling with the dynamical calculations using the multi-dimensional Langevin equation [55]. Three types of the scission configurations in the fission of ^{264}Fm were pointed out as follows: mass-symmetric compact configuration, mass-asymmetric configuration, and mass-symmetric elongated configuration [55]. Further Asano *et al.* [55] calculated the mass-yield and TKE distributions for each type of the scission configurations. Recently, dynamical effects including the dissipation tensor have been taken into account to calculate the mass-yield and TKE distributions in each deformation [56]. Similarly three types of scission configurations in SF of the heavy actinides, elongated symmetric, ordinary asymmetric, and compact symmetric, have been calculated using five-dimensional potential-energy surfaces based on the macroscopic-microscopic model [57].

The average TKE observed in various fission systems is approximately expressed in terms of the Coulomb parameter, $Z_f^2/A_f^{1/3}$, where Z_f indicates the atomic number of the fissioning nuclei. It is known that the formula proposed by Viola *et al.* [58] works very well to reproduce the experimental data for both symmetric and asymmetric fission. Based on the constant β values as discussed, $\beta_{sym} = 1.65$ and $\beta_{asym} = 1.53$, the new empirical formulas have been derived for the TKE release in the fission process [48]:

$$\langle \mathrm{TKE} \rangle_{sym} = 0.1173 \times Z_f^2/A_f^{1/3} + 7.5\ \mathrm{MeV} \quad (1)$$

for the symmetric fission and

$$\langle \mathrm{TKE} \rangle_{asym} = 0.1217 \times Z_f^2/A_f^{1/3} + 3.5\ \mathrm{MeV} \quad (2)$$

for the asymmetric one.

5.2 Mass distributions

Systematic features of the mass-yield and TKE distributions in both symmetric and asymmetric fission depending on A and Z of the fissioning nuclides are discussed in detail by Ohtsuki *et al.* [40] and Zhao *et al.* [48]. The effects of A and Z on the relative probability of either deformation path, and the characteristics of the final mass division phenomena and scission properties resulting from each deformation path, have been extensively studied. Recently, elemental

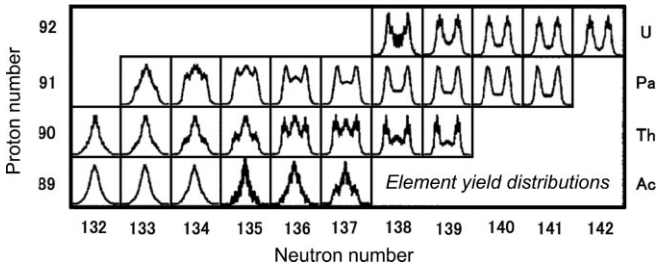

Fig. 11. Fission-fragment elemental yield distributions observed in Coulomb fission are shown on the chart of nuclides. Adapted from [61].

yields of fission fragments in the Coulomb fission have been obtained for a number of neutron-deficient actinides and pre-actinides by using the unique relativistic radioactive beam method by Schmidt *et al.* [59, 60]. The elemental yield distributions after Coulomb fission are depicted as functions of Z and N of the fissioning nuclei in Fig. 11 [61]. The transition from a single-humped mass(element)-yield distribution at ^{221}Ac ($N = 132$) to a double-humped one at ^{234}U ($N = 142$) is clearly seen. In the transition region around ^{227}Th ($N = 137$), triple-humped distributions appear, demonstrating comparable yields for the symmetric and asymmetric fission modes, which is fairly consistent with the feature in Fig. 3 by Ohtsuki *et al.* [20].

Quite recently, a surprising asymmetric fission *via* β-delayed fission has been observed by Andreyev *et al.* [62], in which the proton-rich nuclide ^{180}Hg that is the β-decayed daughter of ^{180}Tl has undergone fission. ^{180}Tl was produced in a spallation reaction with 1.4 GeV proton beams on a UCx target, and was purified through a combination of resonance laser ionization and mass separation in the ISOLDE facility at CERN. The fission-fragment mass distribution is asymmetric with the peaks around A $\sim$ 100 and 80. It should be noted that no asymmetric peak at around $A_H = 140$ was observed. Although this new type of asymmetric fission is inconsistent with the pictures in Figs. 3 and 11, a calculation with the multi-dimensional potential energy surface based on five independent shape parameters suggests that there are two fission paths, symmetric and asymmetric, and they are separated from each other by a ridge and that the entrance to the symmetric valley lies at a much higher excitation energy [62].

Schematic representations of all of the measured mass-yield distributions (normalized to 200% fragment yield) for SF of the trans-Bk isotopes are shown in Fig. 12 as depicted by Hoffman and Lane [63]. It is interesting to observe rather sudden changes from asymmetric to symmetric fission as reflected by the mass distributions which change from asymmetric to symmetric form when the neutron number increases toward $N \approx 160$ for the elements Fm ($Z = 100$), No ($Z = 102$) and Rf ($Z = 104$). Some theoretical approaches to understand characteristic features of SF of heavy actinides have been extensively pursued in [55–57, 64–66].

6. Bimodal fission in heavy actinides

From the above systematic analysis of the deformation at scission, we could interpret the so-called bimodal fission of

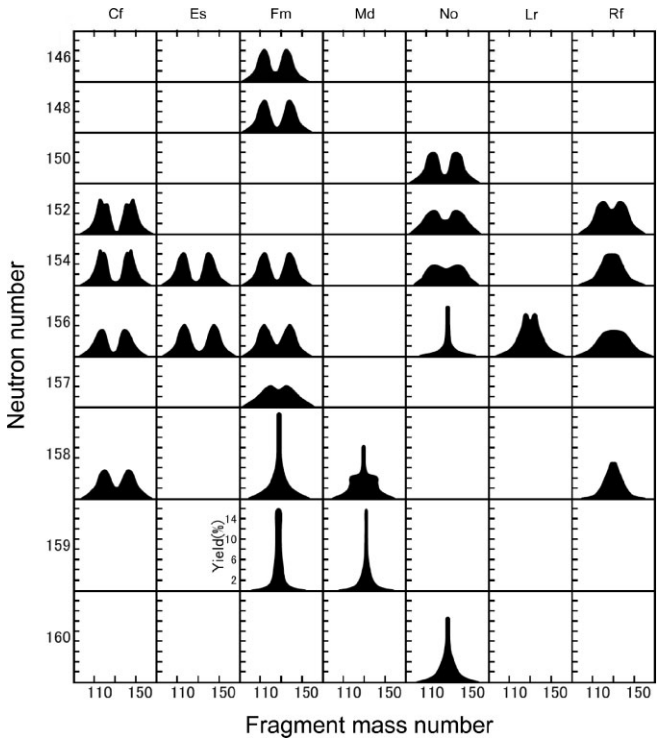

Fig. 12. Schematic representation of all known mass-yield distributions for SF of trans-Bk isotopes. Adapted from [63].

the heavy actinides as essentially the two-mode fission observed in the light actinides. The point of difference between the two-mode and the bimodal fission is the liquid-drop-like elongated symmetric scission-configuration in the two-mode and the compact symmetric-scission configuration due to the strong fragment shell effect in the bimodal fission. The asymmetric fission mode is still competing with the strongly shell affected symmetric fission mode even in the bimodal fission process.

The calculations by Möller *et al.* [31] show the presence of different saddle point configurations for each deformation path to the symmetric and asymmetric fission valleys even in the Fm region. It is interesting to note that the relative heights of the symmetric and the asymmetric barriers are reversed when the neutron number is increased by two units; the saddle leading to the asymmetric valley is lower in the fission of ^{256}Fm whereas it becomes higher than the one leading to the symmetric valley in ^{258}Fm. Thus, there exists a transition point in the height of the saddle from the asymmetric to the symmetric in this region with neutron number around 160. The theoretical results reproduce the systematic change of the mass-yield distributions in Fig. 12.

From the systematic features of the shape elongation at scission and the mass-yield distributions, following remarks are also pertinent. As the barrier penetration phenomena in SF are so sensitively dependent on the height and shape of the fission barriers, the effects of nuclear shell structure of the fissioning nuclides and/or of the fragments are dramatically evident in the observed mass-yield curves; they suddenly change from the ordinary double humped one to a single narrow one by the addition of one neutron to the fissioning nuclide. On the other hand, the shell effects on the scission shape in the symmetric fission valley emerge gradually as a function of N and Z of fissioning nuclides. It should be recognized, however, that such shell effects are not obvious in the fission events that have passed through the deformation path in the asymmetric fission valley.

7. Conclusions and outlook

The two independent deformation paths were experimentally verified in the fission of actinides. It appears that in the low-energy fission of light actinides a nucleus that experiences the higher threshold energy elongates more and results in a stretched scission configuration with preference for symmetric mass-division. On the other hand, the nucleus experiencing the lower threshold energy near the deformation of the outer potential barrier starts to develop the neck and ends up with a compact scission configuration with preference for asymmetric mass-division.

The different scission configurations associated with the two fission modes were found to originate from extremely different degrees of the fragment deformation at the fragment mass number $A \sim 130$. It was also found that the asymmetric fission path still exists even in the bimodal fission of the heavy actinides, while the shell-influenced symmetric fission path is gradually manifested in SF of the heavy actinides. Although multi-scission configurations are predicted and confirmed experimentally, the major fission process would be described as schematically shown in Fig. 1: two fission barriers and the following two fission valleys.

As discovered in the β-delayed fission of ^{180}Hg, it is a good challenge to search for new fission channels in the region of extremely unstable nuclei, such as neutron-deficient, neutron-rich, and proton-excess (superheavy) nuclei. Delayed fission permits such studies of fission properties of nuclides far from stability [67]. It is also worth pointing out that in the fission of superheavy nuclei with $A_f \sim 280$, the two fission valleys, symmetric and asymmetric, may merge into one, due to the mass symmetry leading to the fragments $A \sim 140$ which is affected by the deformed shells ($N = 88$) as observed in the ordinary asymmetric fission [68]. Thus, a mass distribution with a single peak at $A \sim 140$ and with the most probable TKE around 240–250 MeV evaluated from the constancy of β_{asym} would be expected.

Recently, Randrup and Möller have calculated fission-fragment mass distributions using five-dimensional fission potential-energy surfaces in which they treated the nuclear shape evolution in analogy with Brownian motion and performed random walks [69, 70]. The calculations are in good agreement with experimental data of low-energy actinide fission. A number of dynamical models of fission have also been developed using, such as the Langevin approach [71] and the time-dependent Hartree–Fock–Bogoliubov method [66]. Further quantitative interpretation of mass-division mechanism will add considerably to experimental and theoretical studies related to systematic characters of fission.

References

1. Hahn, O., Strassmann, F.: Naturwissenschaften **27**, 11 (1939).
2. Meitner, L., Frisch, O. R.: Nature (London) **143**, 239 (1939).
3. Bohr, N., Wheeler, J. A.: Phys. Rev. **56**, 426 (1939).
4. Vandenbosch, R., Huizenga, J. R.: *Nuclear Fission*. Academic, New York, USA (1973).

5. Wagemans, C. (ed.): *The Nuclear Fission Process*. CRC Press, Boca Raton, USA (1991).
6. Denschlag, J. O.: Nuclear fission. In: *Handbook of Nuclear Chemistry*. 2nd Edn. (Vértes,A., Nagy, S., Klencsár, Z., Lovas, R. G., Rösch, F., eds.) Springer, Dordrecht, The Netherlands (2011), p. 223.
7. Nagame, Y., Zhao, Y. L., Nishinaka, I., Goto, S., Kaji, D., Tanikawa, M., Tsukada, K., Asai, M., Haba, H., Sakama, M., Ichikawa, S., Kudo, H., Nakahara, H.: Radiochim. Acta **89**, 681 (2001).
8. Möller, P.: Nucl. Phys. A **192**, 529 (1972).
9. Ledergerber, T., Pauli, H.-C.: Nucl. Phys. A **207**, 1 (1973).
10. Strutinsky, V. M.: Nucl. Phys. A **95**, 420 (1967).
11. Turkevich, A., Niday, J. B.: Phys. Rev. **84**, 52 (1951).
12. Konecny, E., Schmitt, H. W.: Phys. Rev. **172**, 1226 (1968).
13. Konecny, E., Specht, H. J., Weber, J.: In: Proceedings of the Third IAEA Symposium on the Physics and Chemistry of Fission, IAEA, Vienna, 1974, Rochester (1973), Vol. 2, p. 3.
14. Weber, J., Britt, H. C., Gavron, A., Konecny, E., Wilhelmy, J. B.: Phys. Rev. C **13**, 2413 (1976).
15. Kudo, H., Muramatsu, H., Nakahara, H., Miyano, K., Kohno, I.: Phys. Rev. C **25**, 3011 (1982).
16. Kudo, H., Nagame, Y., Nakahara, H., Miyano, K., Kohno, I.: Phys. Rev. C **25**, 909 (1982).
17. Itkis, M. G., Okolovich, V. N., Smirenkin, G. N.: Nucl. Phys. A **502**, 243c (1989).
18. Ohtsuki, T., Hamajima, Y., Sueki, K., Nakahara, H., Nagame, Y., Shinohara, N., Nakahara, H.: Phys. Rev. C **40**, 2144 (1989).
19. Ohtsuki, T., Nagame, Y., Tsukada, K., Shinohara, N., Baba, S., Hashimoto, K., Nishinaka, I., Sueki, K., Hatsukawa, Y., Hata, K., Sekine, T., Kanno, I., Ikezoe, H., Nakahara, H.: Phys. Rev. C **44**, 1405 (1991).
20. Ohtsuki, T., Nakahara, H., Nagame, Y.: Phys. Rev. C **48**, 1667 (1993).
21. Milton, J. C. D., Fraser, J. S.: Can. J. Phys. **40**, 1626 (1962).
22. Britt, H. C., Wegner, H. E., Gursky, J. C.: Phys. Rev. **129**, 2239 (1963).
23. Balagna, J. P., Ford, G. P., Hoffman, D. C., Knight, J. D.: Phys. Rev. Lett. **26**, 145 (1971).
24. Hulet, E. K., Wild, J. F., Dougan, R. J., Lougheed, R. W., Landrum, J. H., Dougan, A. D., Schädel, M., Hahn, R. L., Baisden, P. A., Henderson, C. M., Dupzyk, R. J., Sümmerer, K., Bethune, G. R.: Phys. Rev. Lett. **56**, 313 (1986).
25. Hulet, E. K., Wild, J. F., Dougan, R. J., Lougheed, R. W., Landrum, J. H., Dougan, A. D., Baisden, P. A., Henderson, C. M., Dupzyk, R. J., Hahn, R. L., Schädel, M., Sümmerer, K., Bethune, G. R.: Phys. Rev. C **40**, 770 (1989).
26. Ohtsuki, T., Nagame, Y., Ikezoe, H., Tsukada, K., Sueki, K., Nakahara, H.: Phys. Rev. Lett. **66**, 17 (1991).
27. Zhao, Y. L., Nishinaka, I., Nagame, Y., Tsukada, K., Sueki, K., Goto, S., Tanikawa, M., Nakahara, H.: J. Radioanal. Nucl. Chem. **255**, 67 (2003).
28. Nagame, Y., Nishinaka, I., Tsukada, K., Oura, Y., Ichikawa, S., Ikezoe, H., Zhao, Y. L., Sueki, K., Nakahara, H., Tanikawa, M., Ohtsuki, T., Kudo, H., Hamajima, Y., Takamiya, K., Chung, Y. H.: Phys. Lett. **B387**, 26 (1996).
29. Nagame, Y., Nishinaka, I., Tsukada, K., Ichikawa, S., Ikezoe, H., Zhao, Y. L., Oura, Y., Sueki, K., Nakahara, H., Tanikawa, M., Ohtsuki, T., Takamiya, K., Nakanishi, K., Kudo, H., Hamajima, Y., Chung, Y. H.: Radiochim. Acta **78**, 3 (1997).
30. Nagame, Y., Nishinaka, I., Zhao, Y. L., Tsukada, K., Ichikawa, S., Qin, Z., Ikezoe, H., Oura, Y., Sueki, K., Nakahara, H., Tanikawa, M., Ohtsuki, T., Goto, S., Kudo, H., Hamajima, Y., Takamiya, K., Nakanishi, K., Baba, H.: J. Radioanal. Nucl. Chem. **239**, 97 (1999).
31. Möller, P., Madland, D. G., Sierk, A. J., Iwamoto, A.: Nature (London) **409**, 785 (2001).
32. Pashkevich, V. V.: Nucl. Phys. **A169**, 275 (1971).
33. Brosa, U., Grossmann, S., Müller, A.: Phys. Rep. **197**, 167 (1990).
34. Specht, H. J.: Nukleonika **20**, 717 (1975).
35. Itkis, M. G., Okolovich, V. N., Rusanov, A. Ya., Smirenkin, G. N.: Sov. J. Nucl. Phys. **41**, 544 (1985).
36. Cohen, B. L., Ferrell-Bryan, B. L., Coombe, D. J., Hullings, M. K.: Phys. Rev. **98**, 685 (1955).
37. Tsukada, K., Nishinaka, I., Shinohara, N., Ichikawa, S., Nagame, Y., Sueki, K., Nakahara, H., Ohtsuki, T., Tanikawa, M.: Eur. Phys. J. A **2**, 153 (1998).
38. Bohr, A.: In: Proceedings of the First United Nations Conference on the Peaceful Uses of Atomic Energy, Geneva, 1955, United Nations, New York (1956), Vol. 2, p. 151.
39. Halpern, I., Strutinsky, V. M.: In: Proceedings of the Second United Nations International Conference on the Peaceful Uses of Atomic Energy, Geneva, 1958, United Nations, New York (1958), Vol. 15, p. 408.
40. Ohtsuki, T., Nagame, Y., Nakahara, H.: Bimodal nature of nuclear fission. In: *Heavy Elements and Related New Phenomena*. (Greiner, W., Gupta, R. J., eds.) World Scientific, Singapore (1999), Vol. 1, p. 507.
41. Wild, J. F., Aarle, J. van, Westmeier, W., Lougheed, R. W., Hulet, E. K., Moody, K. J., Dougan, R. J., Koop, E.-A., Glaser, R. E., Brandt, R., Patzelt, P.: Phys. Rev. C **41**, 640 (1990).
42. Balagna, J. P., Farrell, J. A., Ford, G. P., Hemmendinger, A., Hoffman, D. C., Veeser, L. R., Wilhelmy, J. B.: In: Proceedings of the Third IAEA Symp. on Physics and Chemistry of Fission (IAEA, Vienna, 1974), Vol. 2, p. 191, Rochester (1973).
43. Hoffman, D. C., Ford, G. P., Balagna, J. P., Veeser, L. R.: Phys. Rev. C **21**, 637 (1980).
44. Nishinaka, I., Nagame, Y., Tsukada, K., Ichikawa, S., Ikezoe, H., Tanikawa, M., Zhao, Y. L., Sueki, K., Nakahara, H.: Phys. Rev. C **70**, 014609 (2004).
45. Terrell, J.: Phys. Rev. **127**, 880 (1962).
46. Möller, P., Sierk, A. J., Ichikawa, T., Iwamoto, A., Bengtsson, R., Uhrenholt, H., Åberg, S.: Phys. Rev. C **79**, 064304 (2009).
47. Zhao, Y. L., Nishinaka, I., Nagame, Y., Tanikawa, M., Tsukada, K., Ichikawa, S., Sueki, K., Oura, Y., Ikezoe, H., Mitsuoka, S., Kudo, H., Ohtsuki, T., Nakahara, H.: Phys. Rev. Lett. **82**, 3408 (1999).
48. Zhao, Y. L., Nagame, Y., Nishinaka, I., Sueki, K., Nakahara, H.: Phys. Rev. C **62**, 014612 (2000).
49. Davies, K. T. R., Sierk, A. J., Nix, J. R.: Phys. Rev. C **28**, 679 (1983).
50. Hulet, E. K.: Phys. Atom. Nucl. **57**, 1165 (1994).
51. Hamilton, T. M., Gregorich, K. E., Lee, D. M., Czerwinski, K. R., Hannink, N. J., Kacher, C. D., Kadkhodayan, B., Kreek, S. A., Nurmia, M. J. Lane, M. R., Neu, M. P., Türler, A., Hoffman, D. C.: Phys. Rev. C **46**, 1873 (1992).
52. Lane, M. R., Gregorich, K. E., Lee, D. M., Mohar, M. F., Hsu, M., Kacher, C. D., Kadkhodayan, B., Neu, M. P., Stoyer, N. J., Sylwester, E. R., Yang, J. C., Hoffman, D. C.: Phys. Rev. C **53**, 2893 (1996).
53. Düllmann, Ch. E., Türler, A.: Phys. Rev. C **77**, 064320 (2008).
54. Haba, H. Kaji, D., Kikunaga, H., Kudou, Y., Morimoto, K., Morita, K., Ozeki, K., Sumita, T., Yoneda, A., Kasamatsu, Y., Komori, Y., Ooe, K., Shinohara, A.: Phys. Rev. C **83**, 034602 (2011).
55. Asano, T., Wada, T., Ohta, M., Ichikawa, T., Yamaji, S., Nakahara, H.: J. Nucl. Radiochem. Sci. **5**, 1 (2004).
56. Asano, T., Wada, T., Ohta, M., Yamaji, S., Nakahara, H.: J. Nucl. Radiochem. Sci. **7**, 7 (2006).
57. Ichikawa, T., Iwamoto, A., Möller, P.: Phys. Rev. C **79**, 014305 (2009).
58. Viola, V. E., Kwiatkowski, K., Walker, M.: Phys. Rev. C **31**, 1550 (1985).
59. Schmidt, K.-H., Heinz, A., Clerc, H.-G, Blank, B., Brohm, T., Czajkowski, S., Donzaud, C., Geissel, H., Hanelt, E., Irnich, H., Itkis, M. G., de Jong, M., Junghans, A., Magel, A., Münzenberg, G., Nickel, F., Pfützner, M., Piechaczek, A., Röhl, C., Scheidenberger, C., Schwab, W., Steinhauser, S., Sümmerer, K., Trinder, W., Voss, B., Zhdanov, S. V.: Phys. Lett. B **325**, 313 (1994).
60. Schmidt, K.-H., Benlliure, J., Junghans, A. R.: Nucl. Phys. A **693**, 169 (2001).
61. Schmidt, K.-H., Steinhäuser, S., Böckstiegel, C., Grewe, A., Heinz, A., Junghans, A. R., Benlliure, J., Clerc, H.-G., de Jong, M., Müller, J., Pfutzner, M., Voss, B.: Nucl. Phys. A **665**, 221 (2000).
62. Andreyev, A. N., Elseviers, J., Huyse, M., Van Duppen, P., Antalic, S., Barzakh, A., Bree, N., Cocolios, T. E., Comas, V. F., Diriken, J., Fedorov, D., Fedosseev, V., Franchoo, S., Heredia, J. A., Ivanov, O., Köster, U., Marsh, B. A., Nishio, K., Page, R. D., Patronis, N., Seliverstov, M., Tsekhanovich, I., Van den Bergh, P.,

Van den Walle, J., Venhart, M., Vermote, S., Veselsky, M., Wagemans, C., Ichikawa, T., Iwamoto, A., Möller, P., Sierk, A. J.: Phys. Rev. Lett. **105**, 252502 (2010).
63. Hoffman, D. C., Lane, M. R.: Radiochim. Acta **70**/**71**, 135 (1995).
64. Warda, M., Egido, J. L., Robledo, L. M., Pomorski, K.: Phys. Rev. C **66**, 014310 (2002).
65. Bonneau, L.: Phys. Rev. C **74**, 014301 (2006).
66. Dubray, N., Goutte, H., Delaroche, J.-P.: Phys. Rev. C **77**, 014310 (2007).
67. Hall, H. L., Hoffman, D. C.: Ann. Rev. Nucl. Part. Sci. **42**, 147 (1992).
68. Wilkins, B. D., Steinberg, E. P., Chasman, R. R.: Phys. Rev. C **14**, 1832 (1976).
69. Randrup, J., Möller, P.: Phys. Rev. Lett. **106**, 132503 (2011).
70. Randrup, J., Möller, P., Sierk, A. J.: Phys. Rev. C **84**, 034613 (2011).
71. Ryabov, E. G., Karpov, A. V., Nadtochy, P. N., Adeev, G. D.: Phys. Rev. C **78**, 044614 (2008).